

Supporting Information for

Large Enhancement of Electrochemical Biomass Oxidation by Optimizing the Competitive Adsorption of HMF and OH⁻ Over Doping of CoO_x

Tianqi Nie,^{a,b} Guihao Liu,^a Ziheng Song,^a Tianyang Shen,^a Xiaoliang Sun,^a Tianrui

Yu,^a Sha Bai,^a Lirong Zheng,^c and Yu-Fei Song^{*ab}

^aState Key Laboratory of Chemical Resource Engineering, Beijing University of Chemical Technology, Beijing 100029, P. R. China. *E-mail: songyf@mail.buct.edu.cn; Fax/Tel: +86 10-64431832.

^bQuzhou Institute for Innovation in Resource Chemical Engineering, Quzhou, Zhejiang Province, 324000 P. R. China.

^cBeijing Synchrotron Radiation Facility, Institute of High Energy Physics, Chinese Academy of Sciences, Beijing 100049, P. R. China.

Section 1. Experimental Detail

Section 2. Experimental Detail Supporting Figures and Tables

Figure S1. HR-TEM images of $\text{CoM}(\text{OH})_x$ (M=Mn, Fe, Co, Ni, Cu and Zn).

Figure S2. XRD patterns of $\text{CoM}(\text{OH})_x$ (M=Mn, Fe, Co, Ni, Cu and Zn)..

Figure S3. HR-TEM images of CoCuO_x .

Figure S4. HR-TEM images of CoMO_x (M=Mn, Fe, Co, Ni, Cu and Zn).

Figure S5. XRD patterns of CoMO_x (M=Mn, Fe, Co, Ni, Cu and Zn).

Figure S6. The XPS spectra of CoMO_x (M=Mn, Fe, Co, Ni, Cu and Zn)..

Figure S7. The Co 2p XPS spectra of CoMO_x (M=Mn, Fe, Co, Ni, Cu and Zn).

Figure S8. Calibration of the saturated Ag/AgCl electrode converted to reverse hydrogen electrode (RHE).

Figure S9. The tafel data of CoMO_x (M=Mn, Fe, Co, Ni, Cu and Zn) for HMFOR.

Figure S10. Nyquist plots of CoMO_x (M=Mn, Fe, Co, Ni, Cu and Zn) for HMFOR.

Figure S11. The LSV plots of HMFOR on CoMO_x (M=Mn, Fe, Co, Ni, Cu and Zn).

Figure S12. HPLC standard curve measurements of a) FDCA; b) HMFCa; c) FFCA; d) HMF; e) DFF; f) The HPLC traces of the products at different concentrations.

Figure S13. Structural characterization of CoCuO_x after HMFOR. a) HR-TEM of CoCuO_x after HMFOR; b) XRD spectra; c) The Co 2p XPS spectra.

Figure S14. Current densities and charge-time during the HMFOR

Figure S15. C_{dl} of CoMO_x (M=Mn, Fe, Co, Ni, Cu and Zn) measured by CVs in 1 M KOH with scan rate of 10 to 50 mV s^{-1} .

Figure S16. Double-layer charging current plotted against the CV scan rate for CoMO_x

(M=Mn, Fe, Co, Ni, Cu and Zn).

Figure S17. LSV curves with normalization by ECSA of CoMO_x in 1 M KOH and 50 mM HMF.

Figure S18. a) Bode plots and b) Nyquist plots of CoCuO_x for OER in different potentials; c) Bode plots and d) Nyquist plots of CoO_x for OER in different potentials.

Figure S19. a) Bode plots and b) Nyquist plots of CoO_x for HMFOR in different potentials.

Figure S20. EPR spectra of CoCuO_x before and after voltage application in 1 M KOH and 50 mM HMF.

Figure S21. Co K-edge EXAFS fitting results for CoMO_x (M=Mn, Fe, Co, Ni, Cu and Zn) (k-space).

Figure S22. Co K-edge EXAFS fitting results for CoMO_x (M=Mn, Fe, Co, Ni, Cu and Zn) (R-space).

Table S1. ICP quantitative analysis of CoO_x doped with different metal elements.

Table S2. HMFOR performance of CoCuO_x and other reported catalysts.

Table S3. The resistance of each component for CoMO_x (M=Mn, Fe, Co, Ni, Cu and Zn) in 1 M KOH and 50 mM HMF.

Table S4. The resistance of each component for CoCuO_x in 1 M KOH.

Table S5. The resistance of each component for CoCuO_x in 1 M KOH with 50 mM HMF.

Table S6. The resistance of each component for CoO_x in 1 M KOH.

Table S7. The resistance of each component for CoO_x in 1 M KOH with 50 mM HMF.

Table S8. Co K-edge EXAFS fitting results for CoMO_x (M=Mn, Fe, Co, Ni, Cu and Zn).

Reference

Section 1. Experimental Detail

Materials. $\text{Co}(\text{NO}_3)_2 \cdot 6\text{H}_2\text{O}$ (99%), $\text{Mn}(\text{NO}_3)_2 \cdot 4\text{H}_2\text{O}$ (99%), $\text{Fe}(\text{NO}_3)_3 \cdot 9\text{H}_2\text{O}$ (99%), $\text{Ni}(\text{NO}_3)_2 \cdot 6\text{H}_2\text{O}$ (99%), $\text{Cu}(\text{NO}_3)_2 \cdot 3\text{H}_2\text{O}$ (99%), $\text{Zn}(\text{NO}_3)_2 \cdot 6\text{H}_2\text{O}$ (99%), NaOH (>98%) and 5-hydroxymethylfurfural (HMF) were all obtained from Energy Chemical and were used directly without any further purification.

Synthesis of $\text{CoM}(\text{OH})_x$ (M=Mn, Fe, Co, Ni, Cu and Zn). The $\text{CoM}(\text{OH})_x$ (M=Mn, Fe, Co, Ni, Cu and Zn) was synthesized using a coprecipitation method according to the reference. A 20.0 ml solution composed 0.75 mmol $\text{Co}(\text{NO}_3)_2 \cdot 6\text{H}_2\text{O}$ and 0.25 mmol $\text{M}(\text{NO}_3)_x \cdot y\text{H}_2\text{O}$ ($\text{Mn}(\text{NO}_3)_2 \cdot 4\text{H}_2\text{O}$, $\text{Fe}(\text{NO}_3)_3 \cdot 9\text{H}_2\text{O}$, $\text{Co}(\text{NO}_3)_2 \cdot 6\text{H}_2\text{O}$, $\text{Ni}(\text{NO}_3)_2 \cdot 6\text{H}_2\text{O}$, $\text{Cu}(\text{NO}_3)_2 \cdot 3\text{H}_2\text{O}$, $\text{Zn}(\text{NO}_3)_2 \cdot 6\text{H}_2\text{O}$) was added drop by drop to a three-necked flask with 20 ml deionized water by a peristaltic pump under magnetic stirring at 80 °C. In the meantime, a solution with 0.25 M NaOH was added to the system to maintain the pH = 10. The precipitates were collected by centrifugation and washed with deionized water for 3 times, ethanol for once. Then 15 mg catalyst was dispersed in 3ml ethanol with the assistance of ultrasonication to form a homogeneous solution. Then 200 μL of the solution was dropped onto a carbon paper (1cm \times 1cm). Taking the sample loss into consideration, the loading of catalyst can be calculated as 1 mg cm⁻².

Synthesis of CoMO_x (M=Mn, Fe, Co, Ni, Cu and Zn). The $\text{CoM}(\text{OH})_x$ was electrochemically oxidized at a scan rate of 50 mV s⁻¹ after forty CV scans.

Characterization. Powder X-ray diffraction (XRD) analysis was recorded on a Bruker D8 diffractometer with Cu-K α radiation. High resolution transmission electron microscopy (HRTEM) images were collected on a JEOL JEM-2010 electron

microscope operating at 200 kV. X-ray photoelectron spectroscopy (XPS) measurements were explored with monochromatized Al K exciting X-radiation (PHI Quantera SXM). XAS measurements were collected using a Lytle detector at the 1W1B station in Beijing Synchrotron Radiation Facility (BSRF). FT-EXAFS shell fitting was carried out with Artemis Software.

Electrochemical measurements. The electrochemical performances were tested in a three-electrode glass cell by a electrochemical workstation (CHI 760e, CH, Shanghai). A method of preparing a work electrode is used as follow: 15 mg $\text{CoM}(\text{OH})_x$ was dispersed in 3ml ethanol with the assistance of ultrasonication to form a homogeneous solution. Then 200 μL of the solution was dropped onto a carbon paper ($1\text{cm} \times 1\text{cm}$). A Pt electrode and a Ag/AgCl electrode were used as counter and reference electrode, respectively. In the hydrazine oxidation reaction, the linear sweep voltammetry (LSV) curves were collected at a scan rate of 5 mV s^{-1} after twenty CV scans. All LSV curves were iR-corrected by using the following formula: $E_{\text{iR-corrected}} = E - I \times R_s$.^[1] The current density differences ($\Delta j = j_a - j_c$) were plotted against scan rates, and the linear slope is twice the double-layer capacitance (C_{dl}). The ECSA can be calculated from the double-layer capacitance (C_{dl}) using the following equation: $\text{ECSA} = S_{\text{geo}} * C_{\text{dl}} / C_s$. Wherein, C_s is specific electrochemical double-layer capacitance and its value in alkaline media is 0.040 mF cm^{-2} , and the S_{geo} represents the geometric surface area of the working electrode.^[2] Operando electrochemical impedance spectroscopy (EIS) tests were measured over a frequency range from 10-1 to 105 Hz with an AC amplitude.

Product characterization. The identification of HMF and corresponding selective oxidation products utilized high-performance liquid chromatography (HPLC, Agilent 1260 Infinity II) equipped with ultraviolet-visible detector and 4.6 mm× 250 mm Agilent 5 HC-C18 column. As for analysis conditions, the wavelength of the UV detector was set to 265 nm, and the mobile phase was methanol and ammonium formate aqueous solution (5 mM, 2:8, flow rate is 0.6 ml min⁻¹). Specifically, 50 μL of electrolyte was removed during potentiostatic electrolysis and diluted to 1 ml with ultrapure water. After evenly diluting, 10 μL of the liquid is injected into the HPLC and separated lasts for 12 minutes.

Section 2. Supporting Figures and Tables

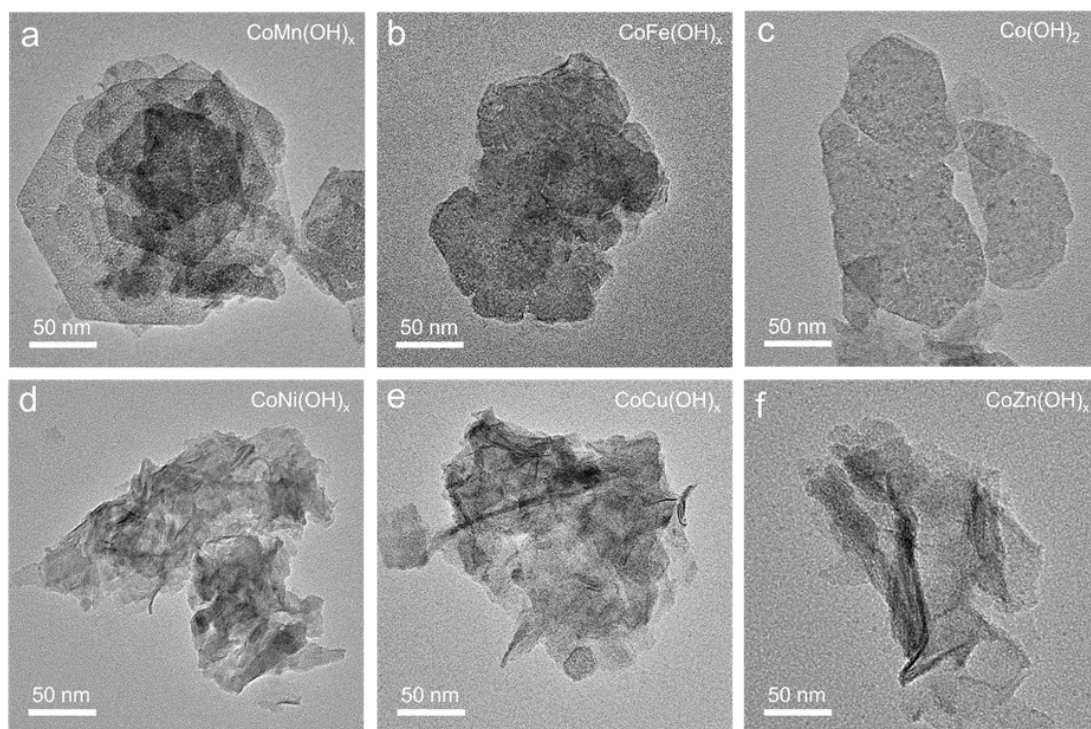


Figure S1. HR-TEM images of CoM(OH)_x ($\text{M}=\text{Mn, Fe, Co, Ni, Cu}$ and Zn).

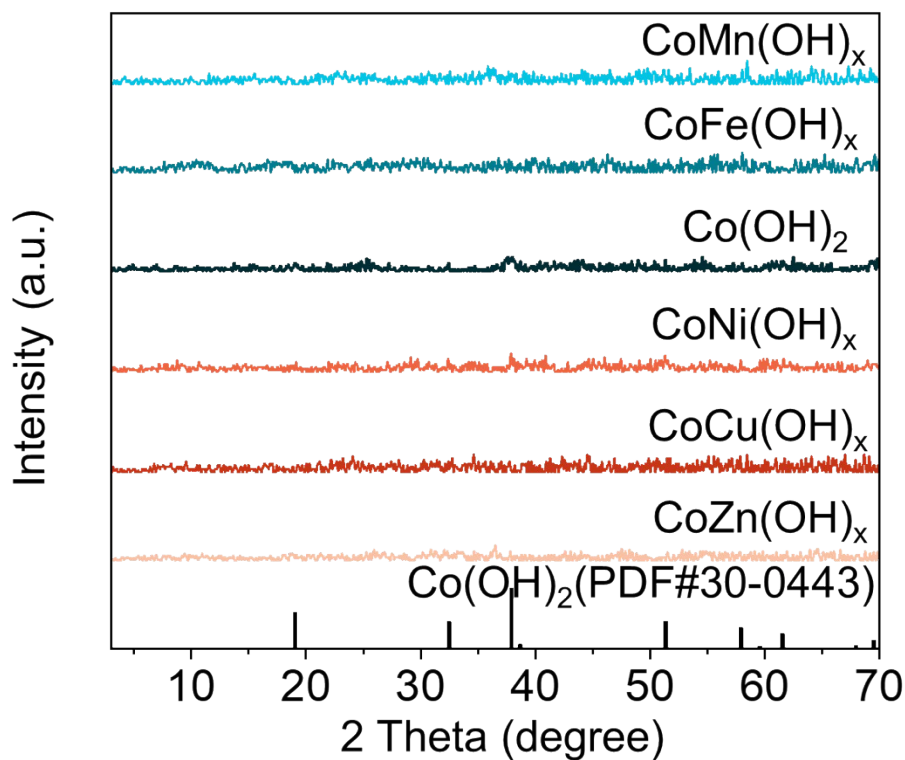


Figure S2. XRD patterns of $\text{CoM}(\text{OH})_x$ ($M=\text{Mn, Fe, Co, Ni, Cu}$ and Zn).

The obtained $\text{CoM}(\text{OH})_x$ sample from co-precipitation exhibited nearly identical sheet-like structures (**Figure S1**). This suggested that the doping of M had no significant influence on the sheet-like structure of $\text{CoM}(\text{OH})_x$. The X-ray diffraction (XRD) patterns were collected to further characterize the crystalline structure of $\text{CoM}(\text{OH})_x$, as shown in **Figure S2**. No significant diffraction peaks were observed, indicating that $\text{CoM}(\text{OH})_x$ had an amorphous structure.^[3]

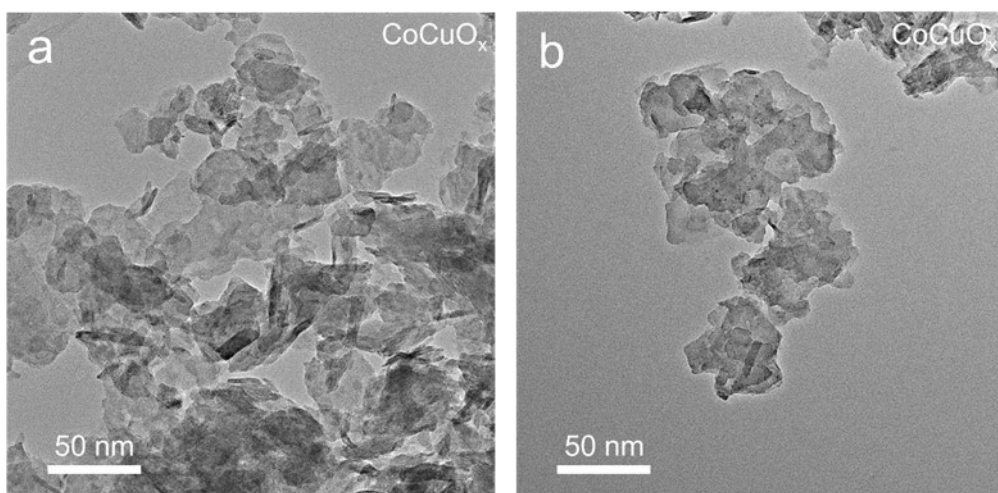


Figure S3. HR-TEM images of CoCuO_x.

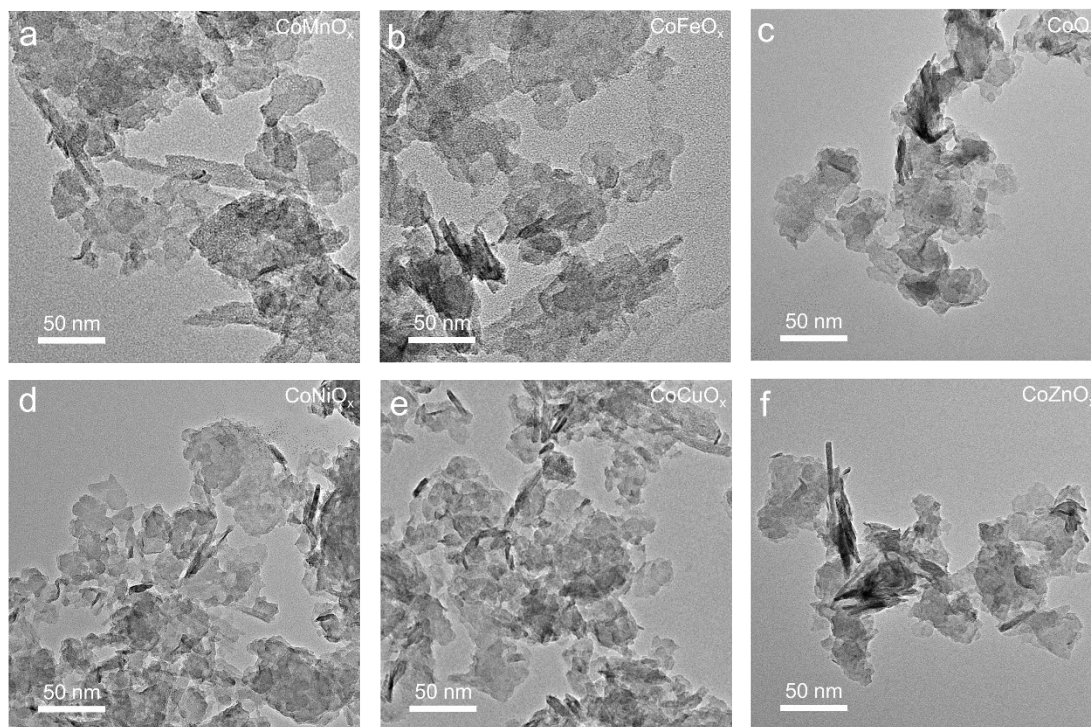


Figure S4. HR-TEM images of CoMO_x (M=Mn, Fe, Co, Ni, Cu and Zn).

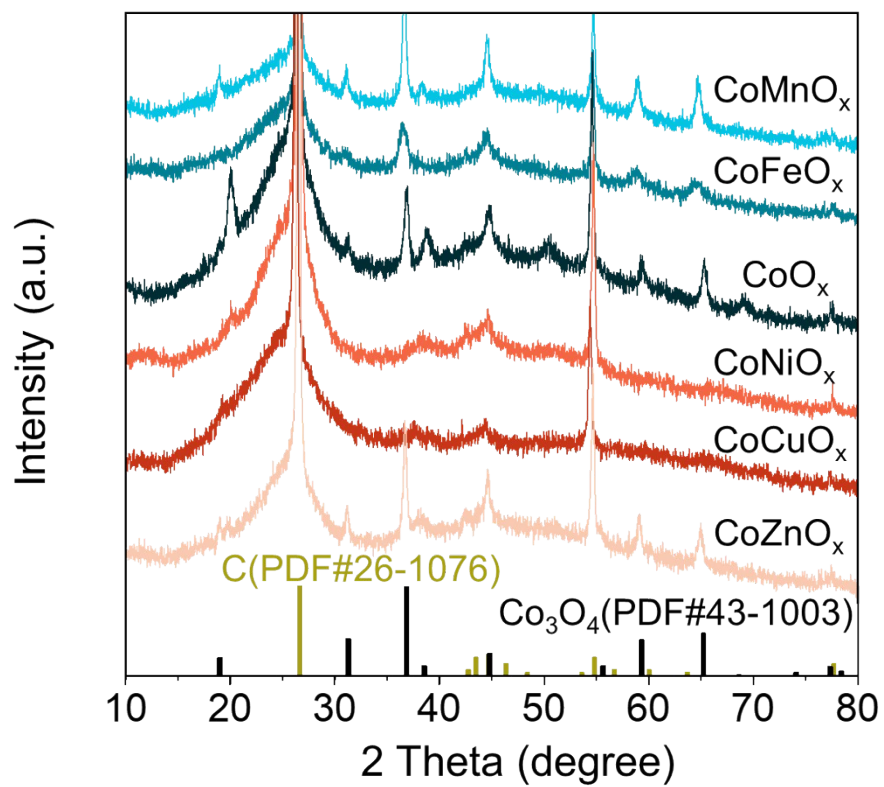


Figure S5. XRD patterns of CoMO_x (M=Mn, Fe, Co, Ni, Cu and Zn).

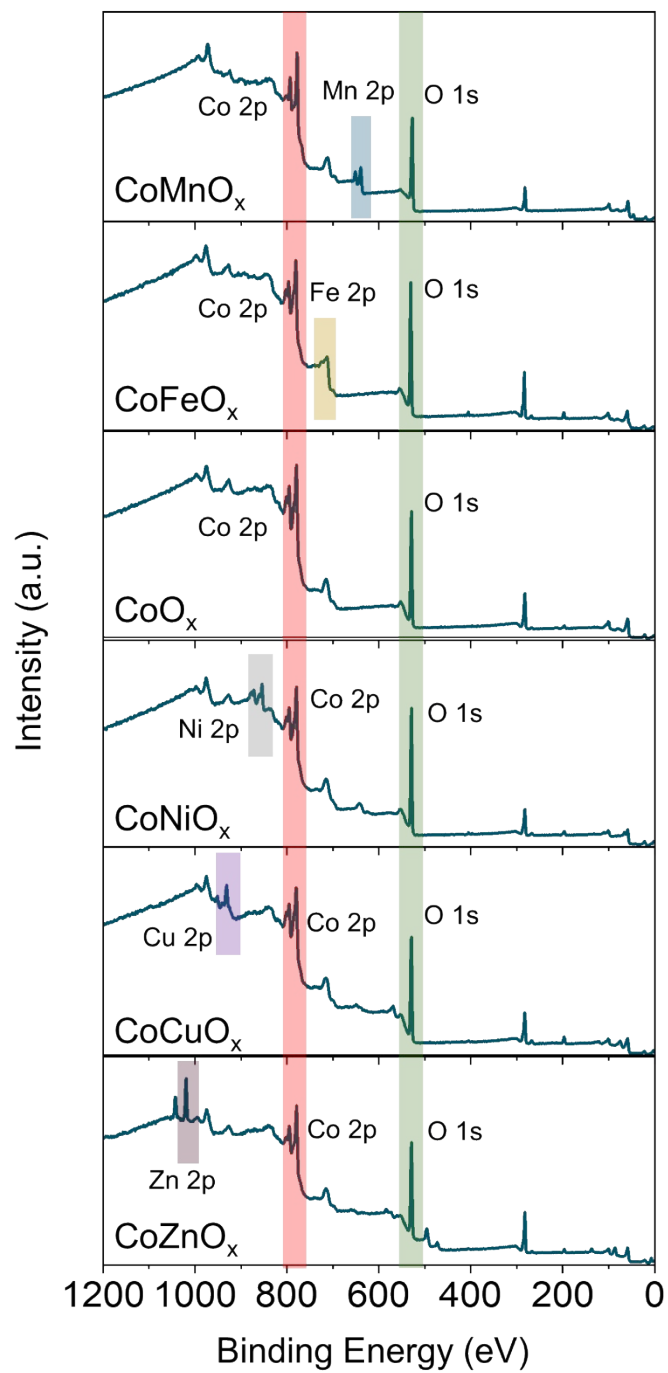


Figure S6. The XPS spectra of CoMO_x (M=Mn, Fe, Co, Ni, Cu and Zn).

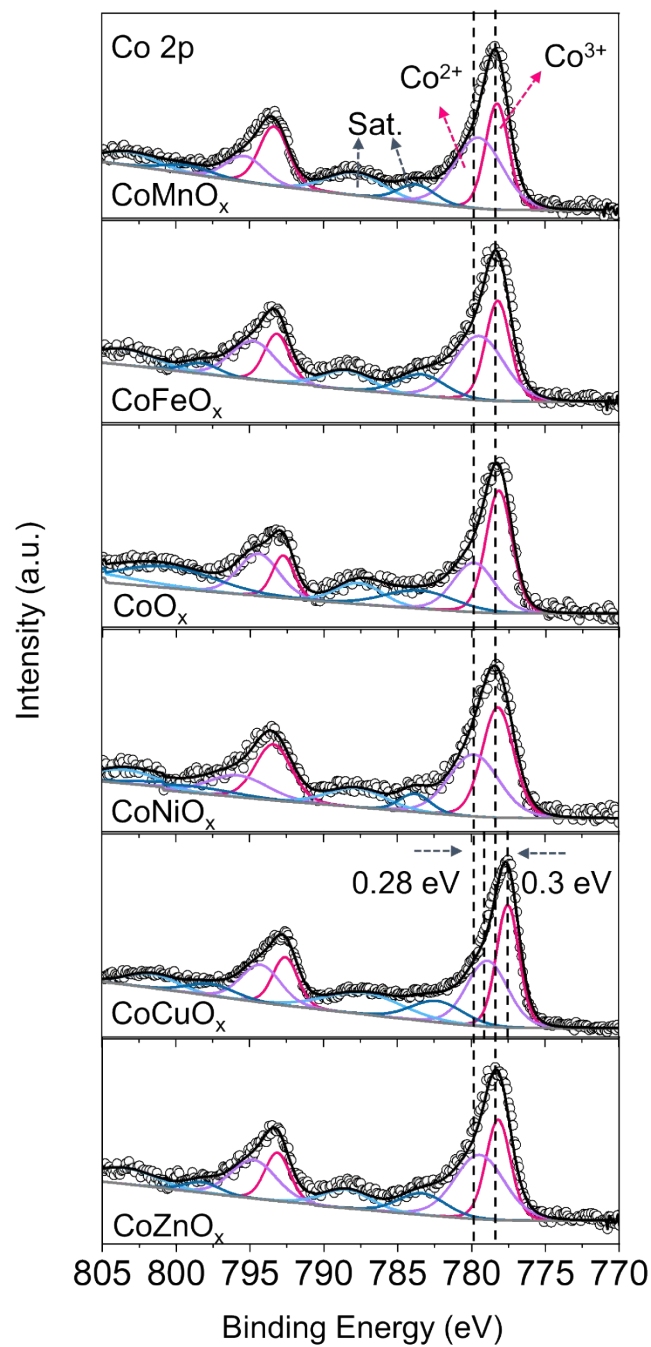


Figure S7. The Co 2p XPS spectra of CoMO_x (M=Mn, Fe, Co, Ni, Cu and Zn).

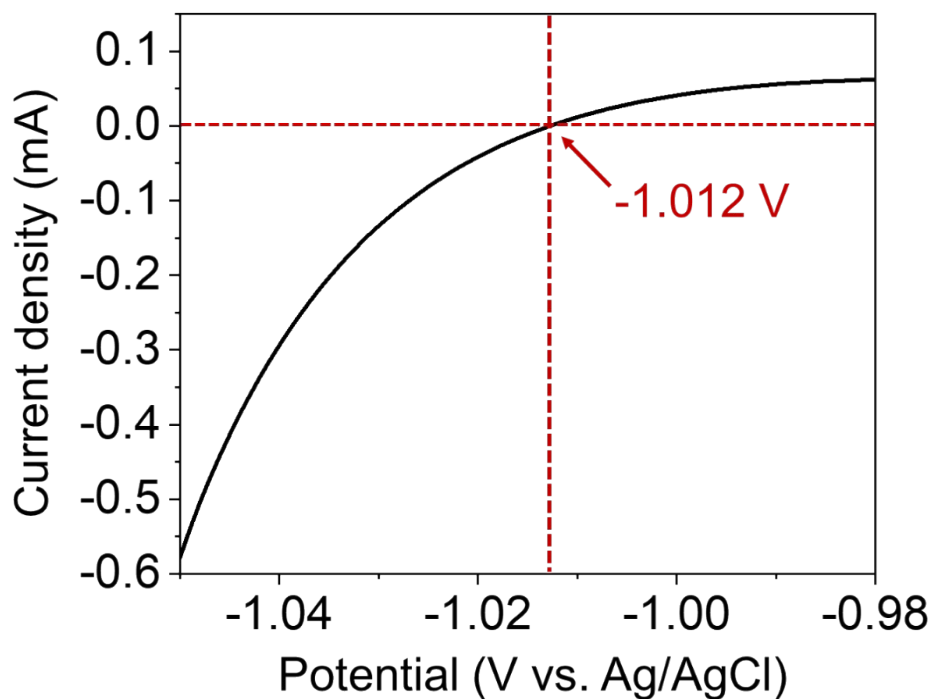


Figure S8. Calibration of the saturated Ag/AgCl electrode converted to reverse hydrogen electrode (RHE). Current-potential curves of the Pt in highly pure H₂-saturated 1.0 M KOH solution with scan rate of 1 mV·s⁻¹. Electrocatalytic OER/HMFOR activity of CoMO_x (M= Mn, Fe, Co, Ni, Cu and Zn), and all the measured polarization curves in this work were converted to reverse hydrogen electrodes (RHE).^[4]

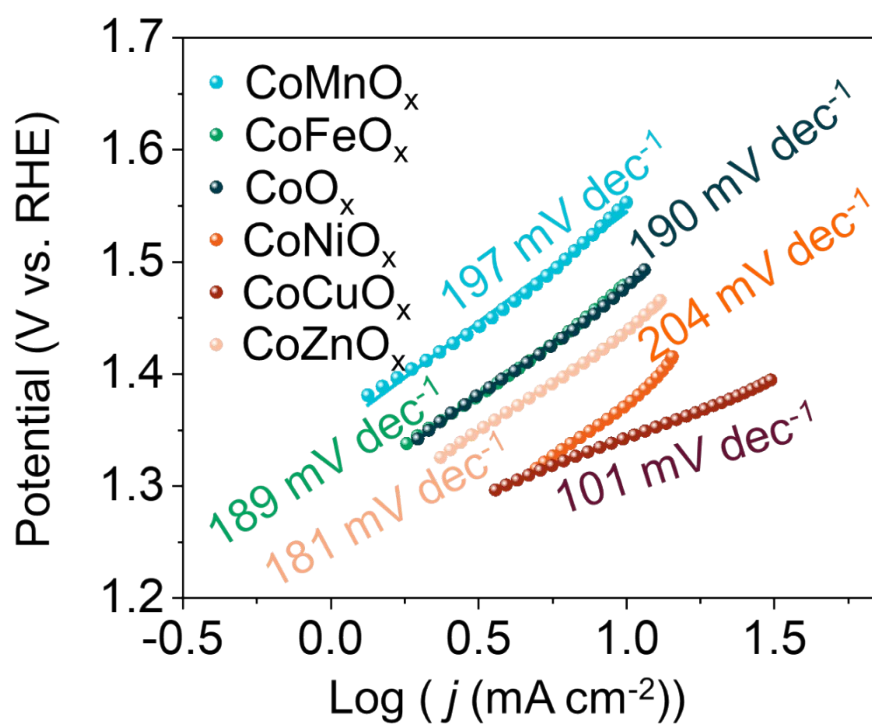


Figure S9. The tafel data of CoMO_x (M=Mn, Fe, Co, Ni, Cu and Zn) for HMFOR.

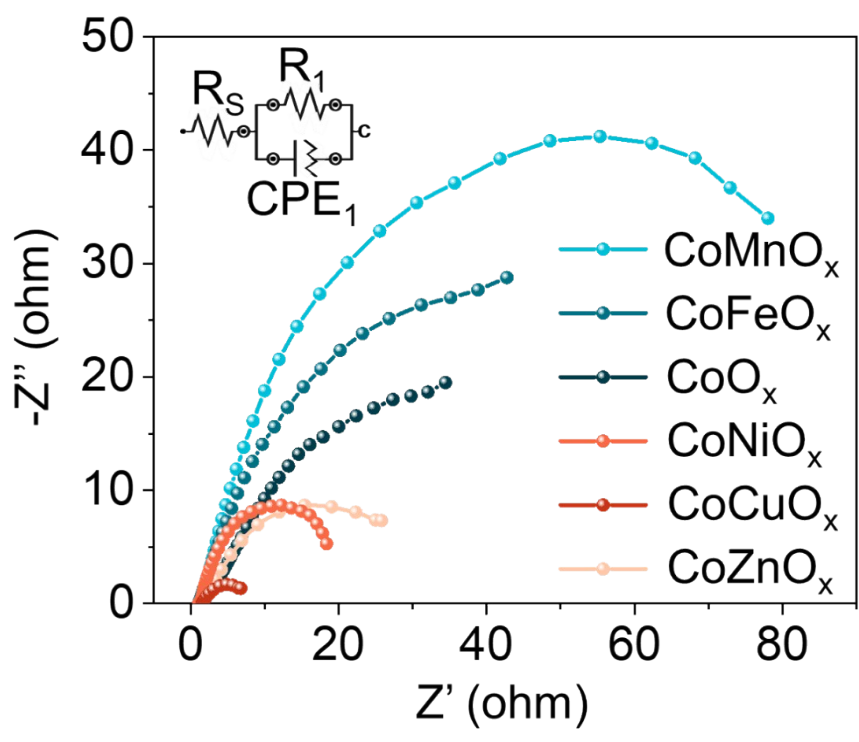


Figure S10. Nyquist plots of CoMO_x (M=Mn, Fe, Co, Ni, Cu and Zn) for HMFOR.

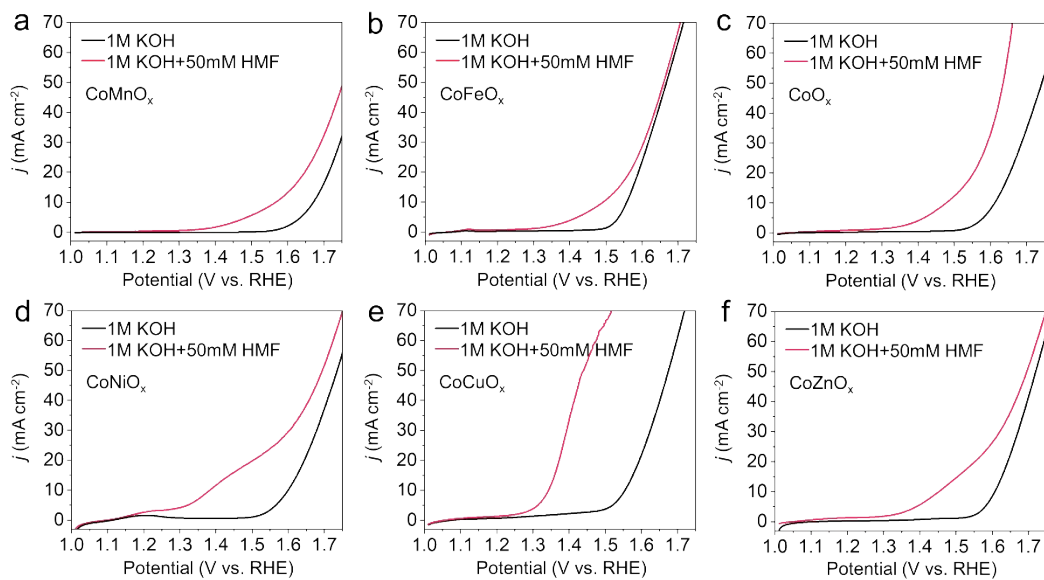


Figure S11. The LSV plots of HMFOR on CoMO_x (M=Mn, Fe, Co, Ni, Cu and Zn).

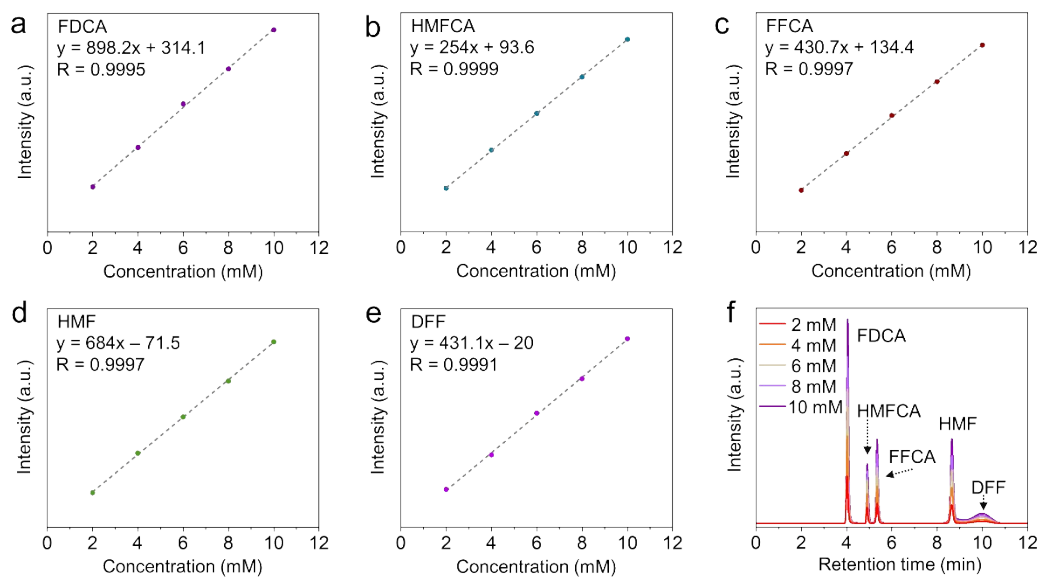


Figure S12. HPLC standard curve measurements of a) FDCA; b) HMFCFA; c) FFCA; d) HMF; e) DFF; f) The HPLC traces of the products at different concentrations.

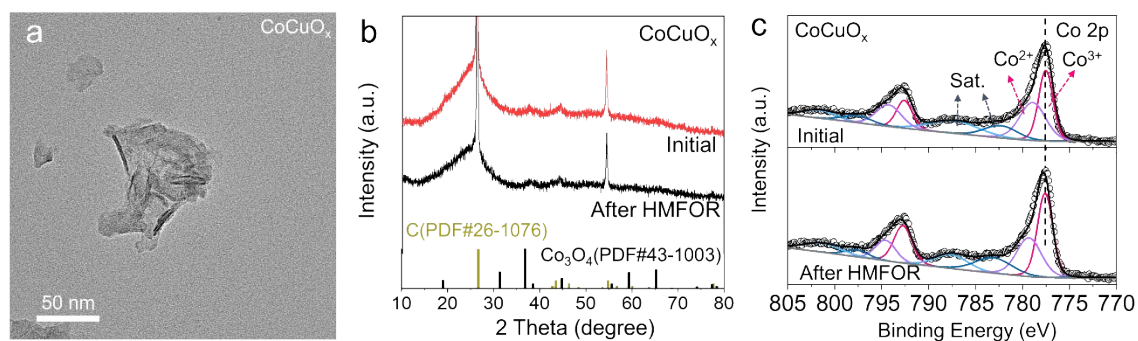


Figure S13. Structural characterization of CoCuO_x after HMFOR. a) HR-TEM of CoCuO_x after HMFOR; b) XRD spectra; c) The Co 2p XPS spectra.

As shown in Figure S13a, the lamellar structure can be observed from the HR-TEM image. Combined with the XRD spectrum, it was evident that the crystal structure of CoCuO_x remained intact before and after the reaction. (Figure S13b). The X-ray photoelectron spectroscopy (XPS) spectra in Figure S13c revealed that the Co binding energies of CoCuO_x were virtually identical, indicating the stability of the valence state of Co before and after the HMFOR reaction. To summarize, the characterization proved the excellent stability of CoCuO_x for HMFOR.

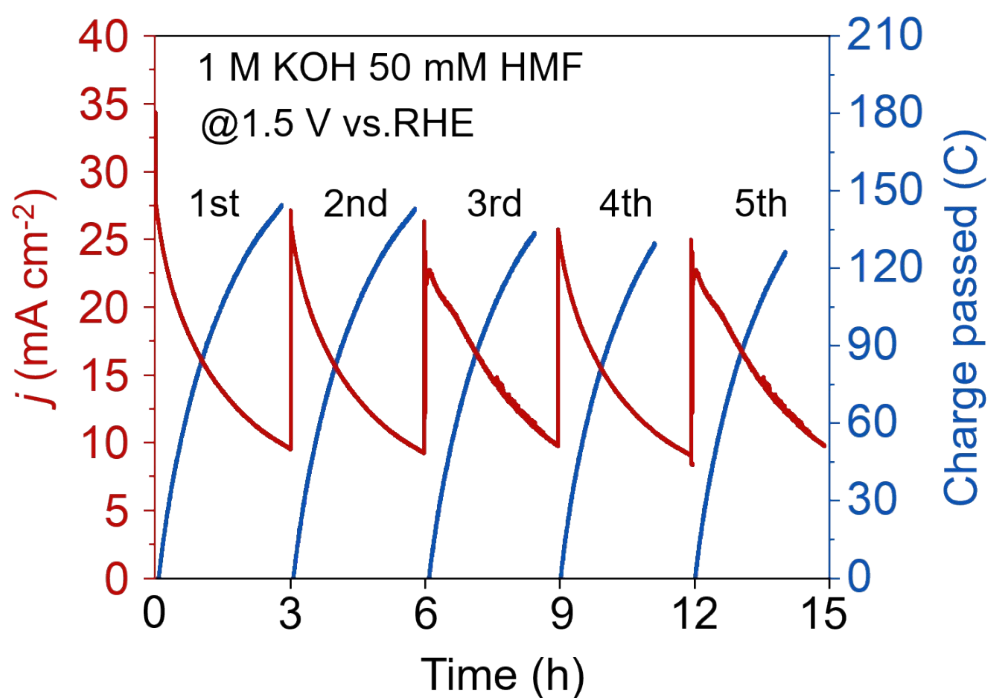


Figure S14. Current densities and charge-time during the HMFOR

As shown in Figure S14, the current density for the HMFOR declined slowly with time because of the consumption of HMF in the electrolyte. After 3 h of the HMFOR, the electrolyte was replaced by a fresh solution (1 M KOH + 50 mM HMF). We found that the starting current density was essentially the same in the following HMFOR cycles, which implied that the CoCuO_x electrode still had high electrochemical activity during long-term HMFOR.

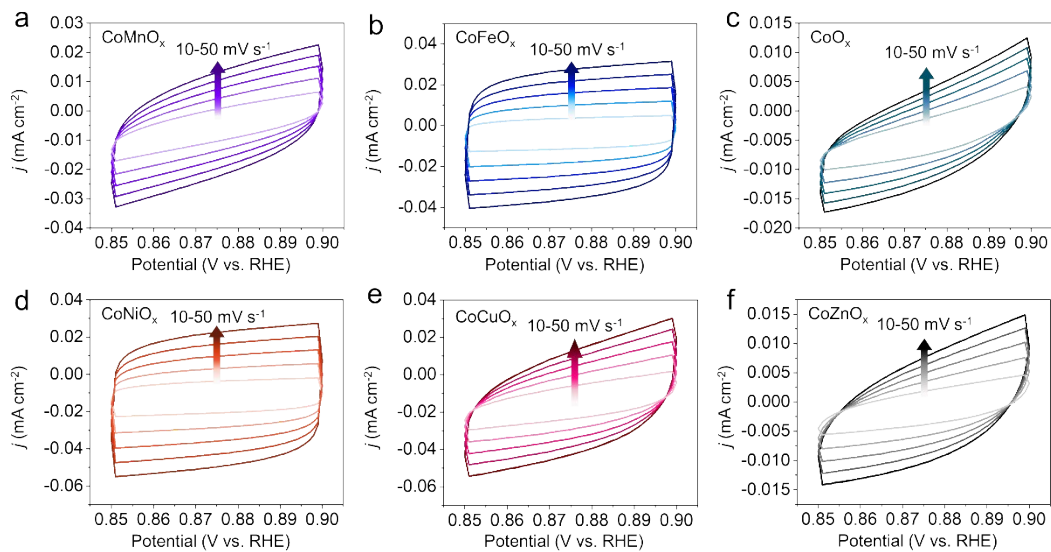


Figure S15. C_{dl} of $CoMO_x$ ($M=Mn, Fe, Co, Ni, Cu$ and Zn) measured by CVs in 1 M

KOH with scan rate of 10 to 50 $mV s^{-1}$.

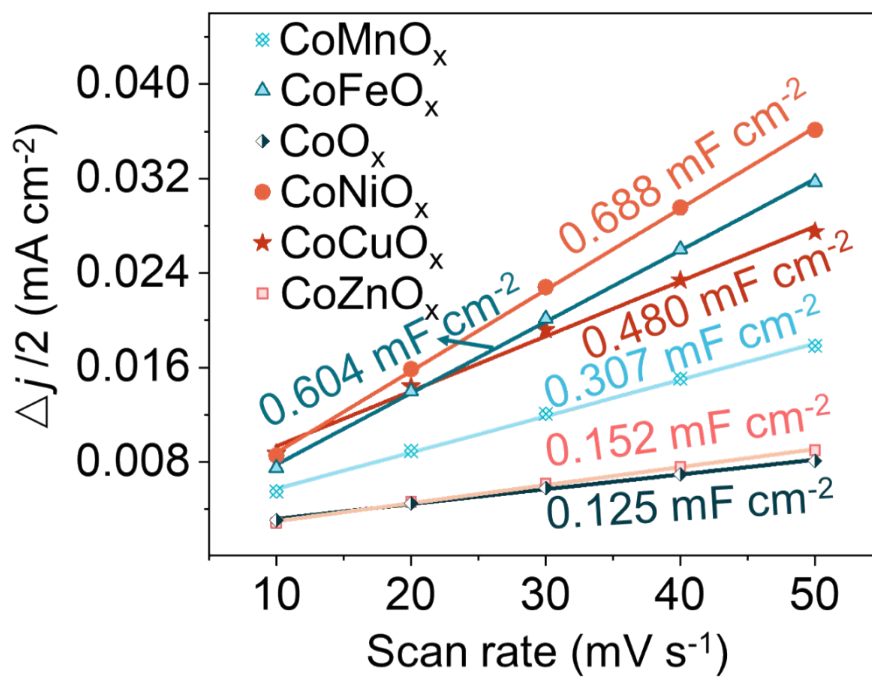


Figure S16. Double-layer charging current plotted against the CV scan rate for CoMO_x

(M=Mn, Fe, Co, Ni, Cu and Zn).

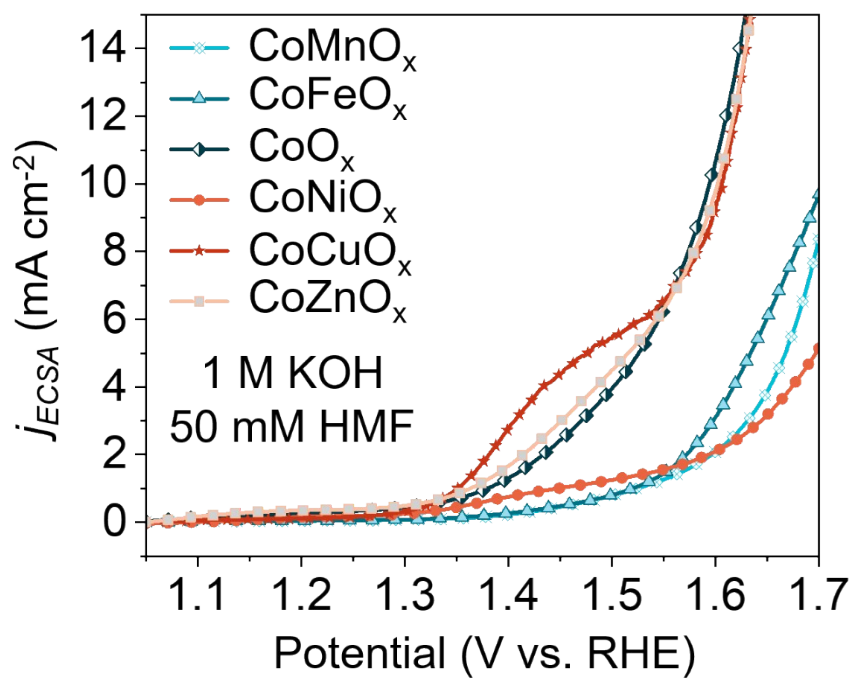


Figure S17. LSV curves with normalization by ECSA of CoMO_x in 1 M KOH and 50 mM HMF.

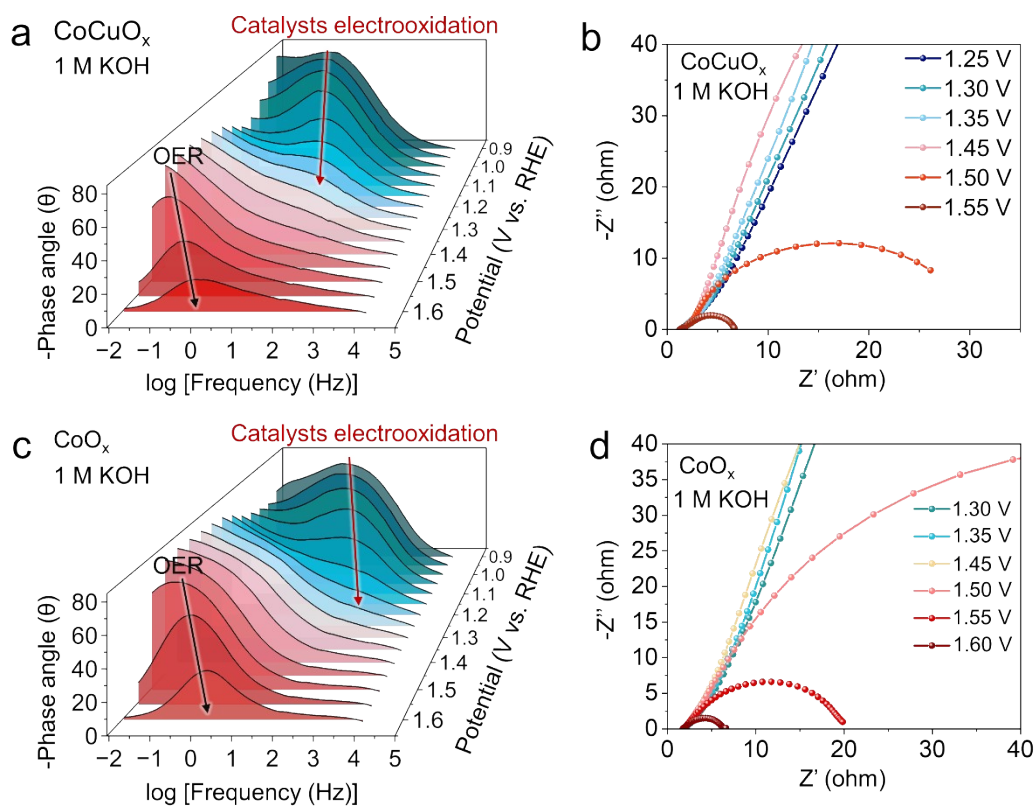


Figure S18. a) Bode plots and b) Nyquist plots of CoCuO_x for OER in different potentials; c) Bode plots and d) Nyquist plots of CoO_x for OER in different potentials.

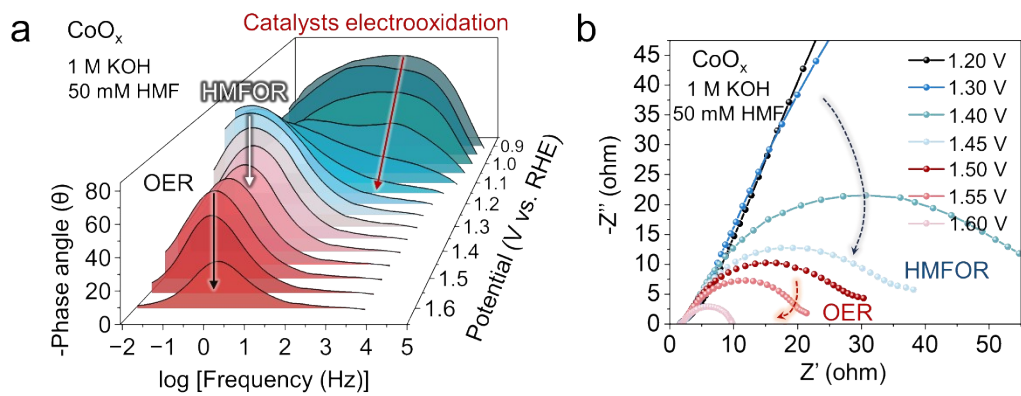


Figure S19. a) Bode plots and b) Nyquist plots of CoO_x for HMFOR in different potentials.

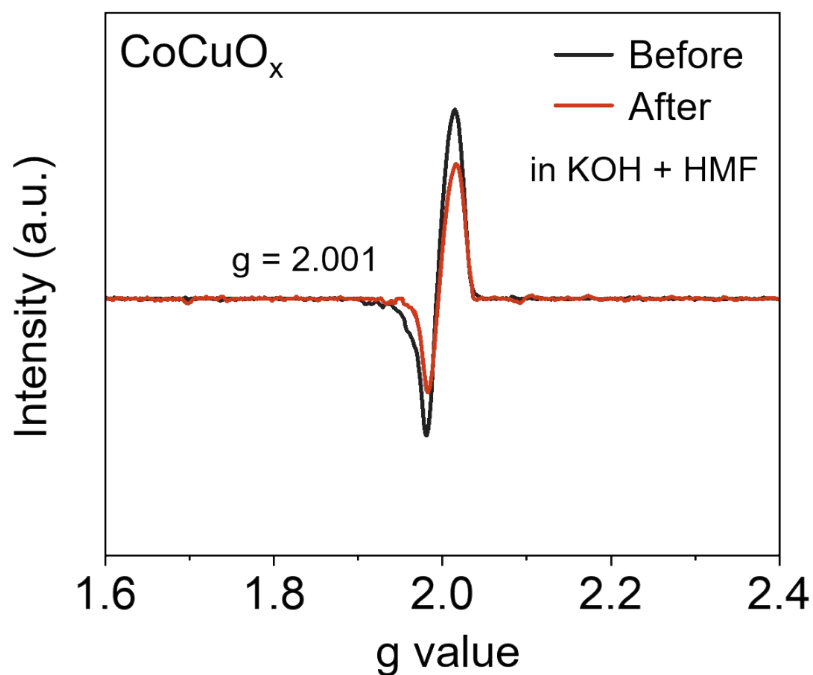


Figure S20. EPR spectra of CoCuO_x before and after voltage application in 1 M KOH and 50 mM HMF.

As shown in Figure S20, a representative EPR signal at $g = 2.001$ was found in CoCuO_x before and after voltage application in 1 M KOH and 50 mM HMF, revealing the electron trapped by oxygen vacancies. The decrease in intensity indicated a reduction in oxygen vacancies, with nucleophilic OH⁻ occupying the oxygen vacancies in CoCuO_x and further participating in HMFOR.

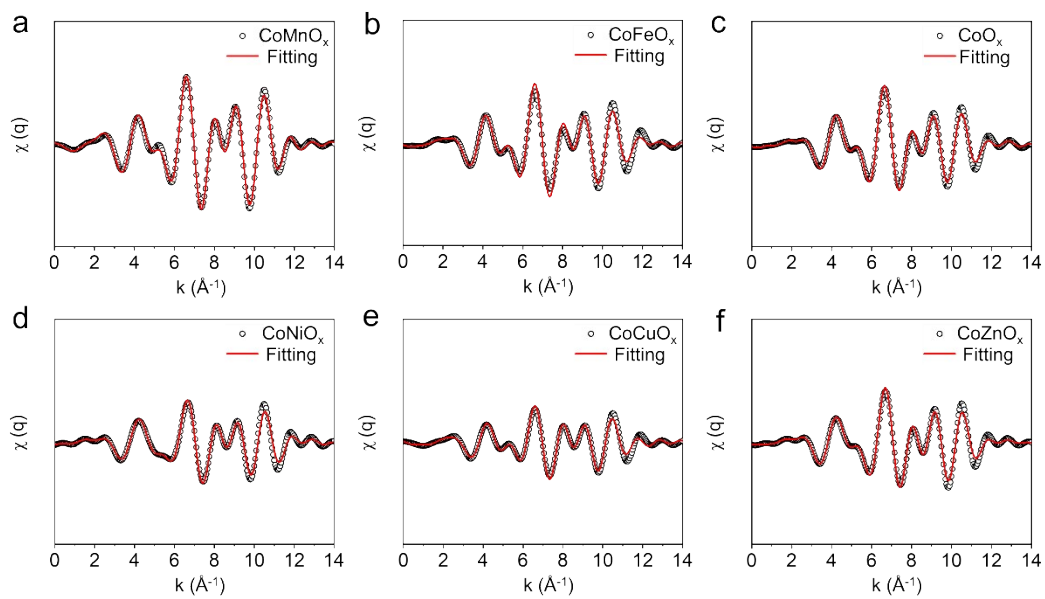


Figure S21. Co K-edge EXAFS fitting results for CoMO_x ($M=\text{Mn, Fe, Co, Ni, Cu}$ and Zn) (k -space).

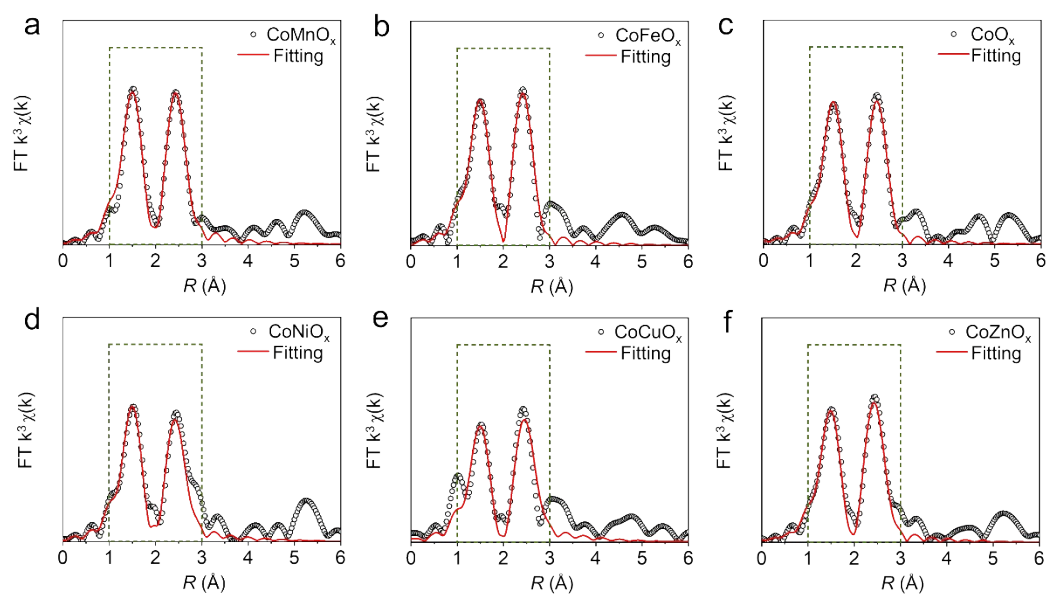


Figure S22. Co K-edge EXAFS fitting results for CoMO_x (M=Mn, Fe, Co, Ni, Cu and Zn) (R-space).

Table S1. ICP quantitative analysis of CoO_x doped with different metal elements.

CoMO_x	M/Co molar ratio	Doped elements (wt.%)
CoMnO _x	0.282	10.10 (Mn)
CoFeO _x	0.302	9.28 (Fe)
CoO _x	/	/
CoNiO _x	0.302	7.58 (Ni)
CoCuO _x	0.313	9.90 (Cu)
CoZnO _x	0.286	8.92 (Zn)

Table S2. HMFOR performance of CoCuO_x and other reported catalysts.

Electrocatalyst	HMF(mM)	*Onset potential (V)	E _{j10} (V)	Ref.
CoCuO_x	50	1.20	1.34	This work
NiCoFe LDH	50	1.32	>1.40	ACS Catal. 2020, 10, 5179
V _O -Co ₃ O ₄	50	1.32	1.35	Adv. Mater. 2022, 34, 2107185
d-NiFe LDH/CP	10	1.42	>1.45	ACS Sustainable Chem. Eng. 2022, 10, 645
NiB _x -P _{0.07}	10	1.49	>1.65	Ind. Eng. Chem. Res. 2020, 59, 17348.
CoFe@NiFe LDH	10	1.28	1.31	Adv. Funct. Mater. 2021, 31, 2102886
Ni ₃ N/C	10	1.30	>1.35	Angew. Chem. Int. Ed. 2019, 58, 15895
PdO-CuO	50	1.22	>1.35	Adv. Mater. 2022, 34, 2204089
hcp-Ni	10	>1.30	>1.40	Angew. Chem. Int. Ed. 2020, 59, 15487
NiCo ₂ O ₄	5	>1.25	>1.40	Appl. Catal. B- Environ. 2019, 242,85.
Ni ₂ S ₃	10	>1.30	>1.35	J. Am. Chem. Soc. 2016, 138, 13639.
Pt (11.9 wt.%)/Ni(OH) ₂	50	>1.30	>1.35	Angew. Chem. Int. Ed 2021, 60, 22908
Ir (7.97 wt%)/Co ₃ O ₄	50	1.20	>1.35	Adv. Mater. 2021, 33, 2007056
P-HEOs	50	>1.30	>1.50	Angew. Chem. Int. Ed. 2021, 60, 20253
Ni(NS)/CP	5	>1.25	>1.40	Angew. Chem. Int. Ed. 2021, 60, 14528
3%Co-NiO/CC	10	1.25	1.35	Chem. Eng. J. 2022, 433,133842
Cr-Ni(OH) ₂ /NF	10	>1.30	>1.35	Appl. Catal. B Environ. 2023, 330, 122590
1.2% Cr-Co-P	10	>1.25	>1.40	Green Chem., 2023, 25, 8196-8206

NOTE: *Onset potential defined here as the HMFOR potential at a current density of 2 mA cm⁻². All the potentials in the table are converted into the reversible hydrogen electrode (RHE).

Table S3. The resistance of each component for CoMO_x (M=Mn, Fe, Co, Ni, Cu and Zn) in 1 M KOH and 50 mM HMF.

CoMO _x	R _s (Ω)	R ₁ (Ω)	CPE _{1-T} (S·s ⁿ ·cm ⁻²)	CPE _{1-P}
CoMnO _x	1.438	111.1	0.006532	0.81544
CoFeO _x	1.103	85.12	0.014559	0.74955
CoO _x	1.882	65.12	0.022118	0.64923
CoNiO _x	1.145	23.05	0.020674	0.80477
CoCuO _x	1.547	6.557	0.05868	0.60269
CoZnO _x	1.46	34.8	0.053756	0.59102

Note: n=CPE-P.

Table S4. The resistance of each component for CoCuO_x in 1 M KOH.

Potential (V)	R _s (Ω)	R ₁ (Ω)	CPE _{1-T} (S·s ⁿ ·cm ⁻²)	CPE _{1-P}	R ₂ (Ω)	CPE _{2-T} (S·s ⁿ ·cm ⁻²)	CPE _{2-P}
0.9	1.949	48891	0.003786	0.87112			
0.95	1.815	10344	0.004076	0.80675			
1	1.678	6916	0.004994	0.69985			
1.05	1.531	3991	0.009052	0.58077			
1.1	1.813	50.23	0.013037	0.72922	8755	0.030876	0.63943
1.15	1.801	48.02	0.019953	0.59515	7831	0.065503	0.75859
1.2	1.786	44.53	0.02692	0.54906	6798	0.075238	0.81456
1.25	1.785	40.57	0.033373	0.52413	5963	0.078647	0.84338
1.3	1.81	34.52	0.046755	0.44995	5102	0.082821	0.84332
1.35	1.777	30.81	0.058554	0.46337	4012	0.11982	0.88564
1.4	1.776	24.63	0.086769	0.42443	3021	0.18315	0.89934
1.45	1.78	19.53	0.12943	0.38846	2513	0.23126	0.89093
1.5	1.834	4.632	0.093561	0.47249	120	0.17911	0.84521
1.55	1.82	3.569	0.090118	0.4764	16.54	0.1525	0.85307
1.6	1.85	0.81481	0.021848	0.67523	6.057	0.081441	0.70917

Note: n=CPE-P.

Table S5. The resistance of each component for CoCuO_x in 1 M KOH with 50 mM

HMF.

Potential (V)	R _s (Ω)	R ₁ (Ω)	CPE ₁ -T (S·s ⁿ ·cm ⁻²)	CPE ₁ -P	R ₂ (Ω)	CPE ₂ -T (S·s ⁿ ·cm ⁻²)	CPE ₂ -P
0.9	1.131	11023	0.000828	0.68597			
0.95	1.208	7970	0.001106	0.67477			
1	1.053	6405	0.00252	0.58626			
1.05	1.293	5758	0.006005	0.55944			
1.1	1.496	33.7	0.28706	0.43463	2344	0.012988	0.5939
1.15	1.511	27.02	0.819	0.54982	1902	0.023363	0.5737
1.2	1.453	23.16	0.27865	0.89526	1244	0.03285	0.5337
1.25	1.381	21.98	0.18245	0.94347	219.1	0.043228	0.48597
1.3	1.432	9.35	0.894444	0.92732	48.23	0.04845	0.51923
1.35	1.274	8.96	0.059705	0.74942	27.59	0.2129	0.29139
1.4	1.474	7.687	0.063292	0.63839	25.94	0.59677	0.40168
1.45	1.486	7.121	0.13102	0.54777	21.72	0.26795	0.6518
1.5	1.435	10.27	0.48921	0.9081	52	0.18093	0.44513
1.55	1.493	3.336	0.15483	0.54443	16.02	0.18678	0.80577
1.6	1.458	2.12	0.25455	0.83648	6.206	0.18966	0.45183

Note: n=CPE-P.

Table S6. The resistance of each component for CoO_x in 1 M KOH.

Potential (V)	R _s (Ω)	R ₁ (Ω)	CPE ₁ -T (S·s ⁿ ·cm ⁻²)	CPE ₁ -P	R ₂ (Ω)	CPE ₂ -T (S·s ⁿ ·cm ⁻²)	CPE ₂ -P
0.9	1.137	76372	0.0025003	0.71161			
0.95	0.97272	53546	0.0034068	0.61475			
1	1.042	20299	0.0044909	0.60355			
1.05	1.179	9677	0.0064392	0.62951			
1.1	1.183	5223	0.015333	0.53846			
1.15	0.7478	191.9	0.050939	0.31222	18892	0.05279	0.848
1.2	1.241	176	0.065301	0.42577	16213	0.065775	0.89849
1.25	1.269	154.5	0.082016	0.42706	14279	0.053794	0.89375
1.3	1.242	139.7	0.14323	0.36649	12896	0.042533	0.87028
1.35	1.287	127.9	0.15082	0.39977	10697	0.052228	0.88607
1.4	1.301	112.3	0.23285	0.37716	9923	0.066014	0.88715
1.45	1.283	102.8	0.416.18	0.31683	8798	0.08941	0.88366
1.5	1.336	76.56	0.40095	0.39145	408.3	0.11211	0.88068
1.55	1.32	35.23	0.093002	0.89727	84.29	0.43366	0.36967
1.6	1.306	1.019	0.31636	0.36691	5.034	0.06427	0.88087

Note: n=CPE-P.

Table S7. The resistance of each component for CoO_x in 1 M KOH with 50 mM

HMF.

Potential (V)	R _s (Ω)	R ₁ (Ω)	CPE ₁ -T (S·s ⁿ ·cm ⁻²)	CPE ₁ -P	R ₂ (Ω)	CPE ₂ -T (S·s ⁿ ·cm ⁻²)	CPE ₂ -P
0.9	1.619	18276	0.0028073	0.86355			
0.95	1.704	14299	0.0035766	0.8176			
1	1.631	11328	0.0042951	0.76822			
1.05	1.482	9291	0.0062796	0.6522			
1.1	1.355	6221	0.011151	0.52752			
1.15	1.705	497	0.2602	0.808	8958	0.003004	0.824
1.2	1.432	202.4	0.036558	0.4244	7989	0.049471	0.784
1.25	1.475	106.3	0.057194	0.39841	6534	0.032694	0.72017
1.3	1.48	93.09	0.21719	0.28035	3099	0.02524	0.62825
1.35	1.589	21.37	0.044438	0.4648	291	0.035663	0.79981
1.4	1.576	13.8	0.060548	0.42805	95.38	0.040877	0.7744
1.45	1.548	12.567	0.10799	0.3547	67.17	0.057095	0.71233
1.5	1.515	13.7	0.19129	0.28342	72	0.064962	0.66555
1.55	1.593	8.56	0.074254	0.40947	38.09	0.06904	0.85659
1.6	1.605	6.86	0.063996	0.42883	14.49	0.059014	0.84692

Note: n=CPE-P.

Table S8. Co K-edge EXAFS fitting results for CoMO_x (M=Mn, Fe, Co, Ni, Cu and Zn).

Sample	Shell	N	R/Å	$\sigma^2/(10^{-3}\text{Å}^2)$	ΔE_0	R-factor
CoMnO _x	Co-O	5.68	1.91	4.2	-2.9	0.013
	Co-M	5.14	2.83	4.0	-5.1	
CoFeO _x	Co-O	4.32	1.91	4.3	-2.2	0.019
	Co-M	4.62	2.85	5.6	-1.8	
CoO _x	Co-O	4.11	1.91	4.3	0.8	0.020
	Co-M	4.31	2.84	7.0	-2.1	
CoNiO _x	Co-O	3.61	1.91	4.2	-2.0	0.009
	Co-M	3.14	2.80	4.4	-4.5	
CoCuO _x	Co-O	3.12	1.92	4.9	-1.3	0.009
	Co-M	2.92	2.83	5.7	-2.5	
CoZnO _x	Co-O	3.85	1.90	4.4	-0.2	0.017
	Co-M	4.22	2.81	6.9	-3.4	

Reference

- [1] Y. Sun, X. Li, T. Zhang, K. Xu, Y. Yang, G. Chen, C. Li and Y. Xie, Nitrogen-Doped Cobalt Diselenide with Cubic Phase Maintained for Enhanced Alkaline Hydrogen Evolution. *Angew. Chem. Int. Ed.* **2021**, *60*, 21575-21582.
- [2] G. Liu, T. Nie, H. Wang, T. Shen, X. Sun, S. Bai, L. Zheng and Y.-F. Song, Size Sensitivity of Supported Palladium Species on Layered Double Hydroxides for the Electro-oxidation Dehydrogenation of Hydrazine: From Nanoparticles to Nanoclusters and Single Atoms. *ACS Catal.* **2022**, *12*, 10711-10717.
- [3] R. Zhong, P. Wu, Q. Wang, X. Zhang, L. Du, Y. Liu, H. Yang, M. Gu, Z. C. Zhang, L. Huang and S. Ye, Room-Temperature Fabrication of Defective CoO_xH_y Nanosheets with Abundant Oxygen Vacancies and High Porosity as Efficient 5-Hydroxymethylfurfural Oxidation Electrocatalyst. *Green Chem.* **2023**, *25*, 4674-4684.
- [4] H. Sun, C.-W. Tung, Y. Qiu, W. Zhang, Q. Wang, Z. Li, J. Tang, H.-C. Chen, C. Wang and H. M. Chen, Atomic Metal-Support Interaction Enables Reconstruction-Free Dual-Site Electrocatalyst. *J. Am. Chem. Soc.* **2022**, *144*, 1174-1186.